

Bacterial turbulence in gradient confinement

Ningzhe Yan(颜宁哲), Chenliang Xie(谢晨亮), Hao Luo(罗昊), Yanan Liu(刘亚楠), and Guangyin Jing(经光银)
Citation: Chin. Phys. B, 2023, 32 (**11**): 114704. DOI: 10.1088/1674-1056/acea6d
Journal homepage: http://cpb.iphy.ac.cn; http://iopscience.iop.org/cpb

What follows is a list of articles you may be interested in

Particle captured by a field-modulating vortex through dielectrophoresis force

Bing Yan(严兵), Bo Chen(陈波), Zerui Peng(彭泽瑞), and Yong-Liang Xiong(熊永亮)
Chin. Phys. B, 2022, 31 (**3**): 034703. DOI: 10.1088/1674-1056/ac248a

Effect of Joule heating on the electroosmotic microvortex and dielectrophoretic particle separation controlled by local electric field

Bing Yan(严兵), Bo Chen(陈波), Yongliang Xiong(熊永亮), and Zerui Peng(彭泽瑞)
Chin. Phys. B, 2021, 30 (**11**): 114701. DOI: 10.1088/1674-1056/abf108

Diffusion and collective motion of rotlets in 2D space

Daiki Matsunaga, Takumi Chodo, Takuma Kawai
Chin. Phys. B, 2020, 29 (**6**): 064705. DOI: 10.1088/1674-1056/ab8ac3

Non-Stokes drag coefficient in single-particle electrophoresis:New insights on a classical problem

Mai-Jia Liao(廖麦嘉), Ming-Tzo Wei(魏名佐), Shi-Xin Xu(徐士鑫), H Daniel Ou-Yang(歐陽新喬), Ping Sheng(沈平)
Chin. Phys. B, 2019, 28 (**8**): 084701. DOI: 10.1088/1674-1056/28/8/084701

Development of a new correlation to calculate permeability for flows with high Knudsen number

Esmaeil Dehdashti
Chin. Phys. B, 2016, 25 (**2**): 024702. DOI: 10.1088/1674-1056/25/2/024702

SPECIAL TOPIC — Celebrating the 100th Anniversary of Physics Discipline of Northwest University

Bacterial turbulence in gradient confinement

Ningzhe Yan(颜宁哲), Chenliang Xie(谢晨亮), Hao Luo(罗昊), Yanan Liu(刘亚楠)[†], and Guangyin Jing(经光银)[‡]

School of Physics, Northwest University, Xi'an 710127, *China*

(Received 9 June 2023; revised manuscript received 12 July 2023; accepted manuscript online 26 July 2023)

We investigate a novel form of non-uniform living turbulence at an extremely low Reynolds number using a bacterial suspension confined within a sessile droplet. This turbulence differs from homogeneous active turbulences in two or three-dimensional geometries. The heterogeneity arises from a gradient of bacterial activity due to oxygen depletion along the droplet's radial direction. Motile bacteria inject energy at individual scales, resulting in local anisotropic energy fluctuations that collectively give rise to isotropic turbulence. We find that the total kinetic energy and enstrophy decrease as distance from the drop contact line increases, due to the weakening of bacterial activity caused by oxygen depletion. While the balance between kinetic energy and enstrophy establishes a characteristic vortex scale depending on the contact angle of the sessile drop. The energy spectrum exhibits diverse scaling behaviors at large wavenumber, ranging from $k^{-1/5}$ to k^{-1}, depending on the geometric confinement. Our findings demonstrate how spatial regulation of turbulence can be achieved by tuning the activity of driving units, offering insights into the dynamic behavior of living systems and the potential for controlling turbulence through gradient confinements.

Keywords: collective motion, bacterial turbulence, bacterial drop, gradient confinement

PACS: 47.61.–k, 47.63.–b, 47.63.Gd, 47.90.+a **DOI:** 10.1088/1674-1056/acea6d

1. Introduction

Microorganisms can stir the surrounding medium to form disturbance flows by beating their flagella or cilium for locomotion. When these microswimmers move collectively at high density, the disturbed flows exhibit spatiotemporal chaotic vortices at a length scale much larger than the size of individual unit.[1] The spontaneous flow generated by tiny swimmers is fascinating and can be analogous to the inertial turbulence occurring at a large scale with high velocity, i.e., high Reynolds number.[2–5] Bacterial suspension, for example, is recognized as a typical system far from equilibrium, in which the energy is continuously injected at the unit level and collective motion of coordinated individuals occurs.[3,6–9] This living turbulence plays a significant role in mixing enhancement and efficient molecular transport at low Reynolds number, and also facilitates the intracellular communications of the cells in biological systems.[10–16] From the fundamental point of view, the statistical features and laws are extremely interesting for the active flows in the systems with living microorganisms at vanishing Reynolds number.[1,17–20]

The individual bacterium injects the energy into the surrounding fluidic medium in a disordered way, which can be however collected to form ordered moving vortices.[21] Extensive studies have been conducted to understand this phase transition from the statistical point of view.[22,23] This new class of the spontaneous flow also raises questions on whether and how this living turbulence manifests the features and universality reminiscent of energy cascades in inertial turbulence.[3–5,24,25] The isotropic hypothesis, commonly applied to well-developed inertial turbulence, is both reasonable and necessary. However, microorganisms experience heterogeneous nutrient and oxygen supplies, compelling them to dynamically adapt to their environment and inject energy in an anisotropic manner. This raises the question of whether the isotropic assumption remains valid for bacterial turbulence across all scales. Moreover, the theoretical analysis and numerical methods for three-dimensional living turbulence are difficult to be realized by direct imaging under microscope.[26–30] Instead, two-dimensional living turbulence is feasibly observed within homogeneous films or channels.[3,7,24,31–33] Dombrowski *et al.* introduced the dense bacteria into a sessile drop and Hele–Shaw confinement, and reported an interesting collective behavior due to oxygen diffusion dynamics.[6] It is however unclear how or to what extent, the properties and mechanisms of non-uniform living turbulence in bacterial suspensions differ from those of uniform counterparts.

Here, we trap dense bacteria inside sessile drops. This geometry, as a natural habitat for bacteria, generates an inevitable thickness gradient in the vicinity of the contact line. Since the characteristic size of the collective motion of the bacterial population depends on the smallest dimension of the confinement (i.e., thickness), we, therefore, build a non-uniform living turbulence confined in the wedge at the corner of the sessile bacterial drop. Particularly, the air–liquid interface allows the diffusion of oxygen and provides a concentration variation along

[†]Corresponding author. E-mail: yanan.liu@nwu.edu.cn
[‡]Corresponding author. E-mail: jing@nwu.edu.cn

© 2023 Chinese Physical Society and IOP Publishing Ltd

the radial direction of the drop due to the thickness gradient. This coupling of the thickness gradient and oxygen gradient allows a new type of heterogeneous turbulent flow in living bacterial suspension. The high activity of the motile bacteria contributes to the strong fluctuation of the living flows close to the contact line where oxygen is rich. However, the fluctuation increasingly decays due to less oxygen supply when the liquid layer gets thicker toward the drop center. Moreover, it turns out that this living turbulence is locally anisotropic at a unit scale while tends to isotropic at a scale around collective motion. The kinetic energy spectrum here exhibits geometric dependence at large wavenumber region, while a robust scaling $E(k) \sim k^1$ with short wavenumber. This heterogenous turbulence built herein by controlling the activity of self-propelled units, suggests the possible spatial guide for the energy transfer across vortices in living turbulence.

2. Results and discussion

2.1. Non-uniform living turbulence

In our experiments, a specific region near the contact line of a sessile droplet is opted to study the collective behavior of the dense bacteria. Naturally, there is a wedge-shaped confinement between the substrate and the air–liquid interface with a gradually varying height from a few to hundreds of micrometers. A drop of bacterial suspension is transferred onto a horizontal glass slide and is kept within a closed chamber with saturated humidity to avoid the influences of evaporation and external disturbances. According to the wetting hysteresis behavior, drops with three contact angles $\theta_1 = 10^\circ, \theta_2 = 22^\circ$ and $\theta_3 = 33^\circ$ are stably controlled through the subtle experimental setup as sketched in Fig. 1. An inverted microscope equipped with a high-speed camera is used to record the collective behavior of bacteria close to the drop edge, with the focal plane at the drop bottom. The visual field has a size of 696 μm × 695 μm (with 0.34 μm/pixel). As shown in the left panel of Fig. 1, the x and y axes represent the radial direction starting from the contact line and the tangential direction along the contact line, respectively.

Similar to the typical depiction of inertial turbulence, the formation of living turbulence within a wedge-shaped space exhibits numerous distinctive intermittent whirls and jets. To characterize this living turbulence, we perform the particle image velocimetry (PIV) analysis through the PIVlab module in MATLAB[34] to obtain the coarse-grained velocity field of the bacterial suspension, as shown in Fig. 2.

In particular, the vorticity map of the living flow shows an obvious non-uniform feature in the case of $\theta_2 = 22^\circ$ (Fig. 2(b)). Note that, the thickness of the wedge-shaped liquid film reduces to several micros at very close to the edge, which suppresses the motility of the swimming bacteria. In order to understand this heterogeneity, it is then necessary to further investigate the spatial distribution of the turbulent kinetic energy. By using the conventional way, the velocity is decomposed into a time averaged velocity $\overline{\boldsymbol{v}}(\boldsymbol{r})$ and fluctuation velocity $\boldsymbol{v}'(\boldsymbol{r},t)$, where $\overline{(\cdot)}$ denotes the average over time. The mean kinetic energy $\overline{E}_{\mathrm{m}}(\boldsymbol{r})$ and turbulent kinetic energy $\overline{E}_{\mathrm{t}}(\boldsymbol{r})$, are calculated from these two velocity components as

$$\boldsymbol{v}(\boldsymbol{r},t) = \overline{\boldsymbol{v}}(\boldsymbol{r}) + \boldsymbol{v}'(\boldsymbol{r},t), \tag{1}$$

$$\overline{E}_{\mathrm{m}}(\boldsymbol{r}) = \frac{1}{2}\overline{\boldsymbol{v}}^2(\boldsymbol{r}), \tag{2}$$

$$\overline{E}_{\mathrm{t}}(\boldsymbol{r}) = \frac{1}{2}\overline{\boldsymbol{v}}'^2(\boldsymbol{r}). \tag{3}$$

The distributions of turbulent kinetic energy $\overline{E}_{\mathrm{t}}(\boldsymbol{r})$ in three cases are shown in Figs. 3(a)–3(c). It can be seen that the collective motion of bacteria is suppressed in the extremely thin liquid layer very close to the contact line, reflected by the much lower turbulent kinetic energy. Thereafter, the turbulent kinetic energy is more or less uniform distributed in the area away from the contact line in both cases of contact angle $\theta_1 = 10^\circ$ and $\theta_3 = 33^\circ$. However, there is an obvious decay of turbulent kinetic energy in the case of θ_2, in the vicinity of 300 μm away from the contact line.

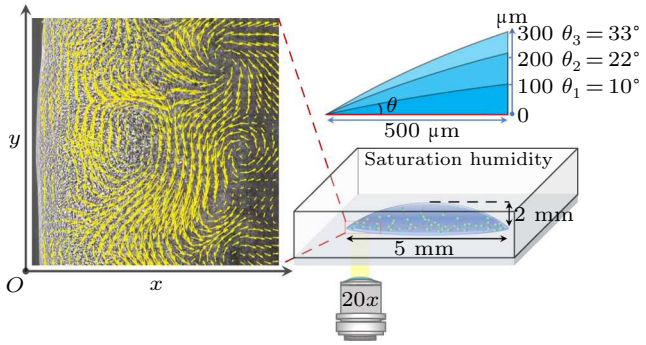


Fig. 1. Sketch of experimental setup. A sessile drop of bacterial suspension with a volume of 5 μL is placed on a cover slide within a saturated humidity chamber. The static equilibrium contact angle of the surface is tuned to be $\theta = 10^\circ$, 22°, 33°, resulting in different gradient confinement. The snapshot of living turbulence near the substrate is recorded and analyzed through the PIV measurements thus obtaining the velocity field as shown on the left panel. Meanwhile, x-axis and y-axis represent the radial and tangential directions of the bacteria droplet, respectively.

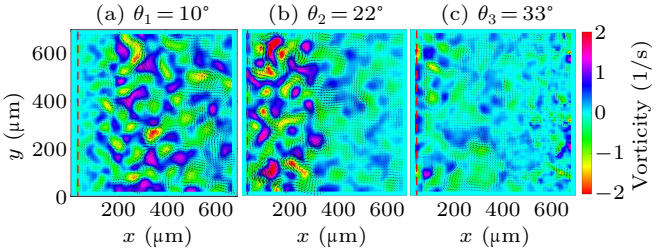


Fig. 2. Velocity fields and vorticity maps of the spontaneous flow of bacterial suspensions close to the contact line with different wedge shapes. From (a) to (c), the velocity field and vorticity map emerge within three confinements by changing the contact angles of 10°, 22°, 33°, respectively. The x and y indicate the radial and tangential directions of the drop, with the origin located at the contact line. The red dotted lines on the left indicate the positions of this contact line.

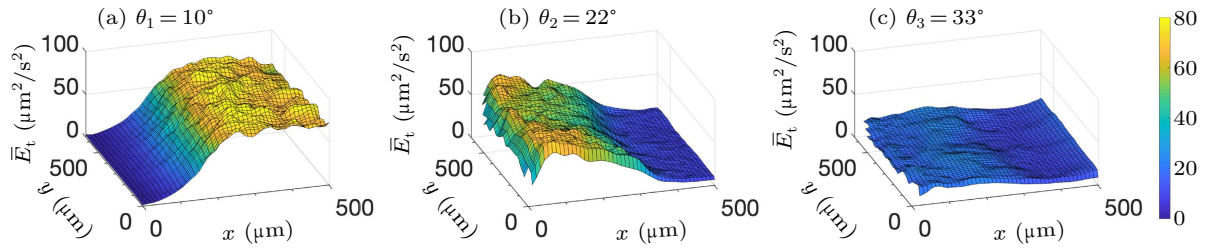


Fig. 3. Distribution of turbulent kinetic energy. (a)–(c) Corresponding distributions of turbulent kinetic energy averaged over 5000 frames (100 s) under three confinements. The color shows the intensity of turbulent kinetic energy $\overline{E}_t$. Meanwhile, $x = 0$ μm indicates the position of the drop contact line.

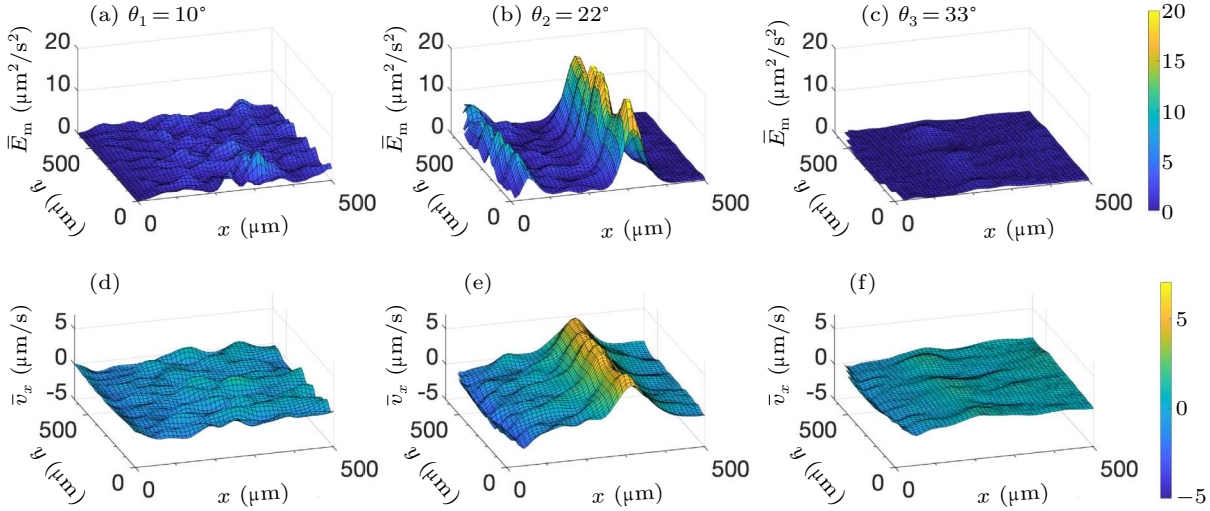


Fig. 4. Mean kinetic energy and velocity $\overline{v}_x$ distributions. (a)–(c) Distributions of the mean kinetic energy $\overline{E}_m$ in three confinements. (d)–(f) Distributions of mean velocity $\overline{v}_x$ in radial direction. Yellow and blue colors represent positive values and negative values, respectively. The distributions are derived from the time average of 5000 frames (100 s).

Interestingly, a remarkable peak appears in the mean kinetic energy distribution in Fig. 4(b) near the position 300 μm away from the drop contact line with $\theta_2 = 22°$. Whereas, other distributions of mean kinetic energy are almost uniform (Figs. 4(a) and 4(c)). Furthermore, we confirm that the peak value of mean kinetic energy results from the contribution of radial velocity $\overline{v}_x$, directing to the inside of the drop, as illustrated in Figs. 4(d)–4(f). The gradient of the turbulent kinetic energy as $\nabla_x \overline{E}_t$ captures the spatial variation of $\overline{E}_t$. This dependence suggests that there is an inward mean flow from the contact line toward the drop center. This inward mean flow requires an outward counterpart above the observation layer (i.e., the substrate bottom in the present work) to form a global circulation, which has been observed in Ref. [35]. The turbulent kinetic energy presents a non-uniform distribution along the radial direction, which is intuitively ascribed to the varying thickness of the wedge-shaped drop corner. Then, we try to figure out the intrinsic reason responsible for the non-uniform fluctuation of turbulent energy. It is measured that the maximum variation of turbulence occurs at the distance about $x = 300$ μm away from the contact line, as shown in Figs. 4(b) and 4(e). We confirm that this distance is stable around the whole drop by repetitively independent experiments. This characteristic distance corresponds to the local liquid height at that position, which establishes a vertical diffusion layer for oxygen. The bottom layer of the drop experiences a limited oxygen supply, whereas the air–liquid interface benefits from a rich oxygen source.

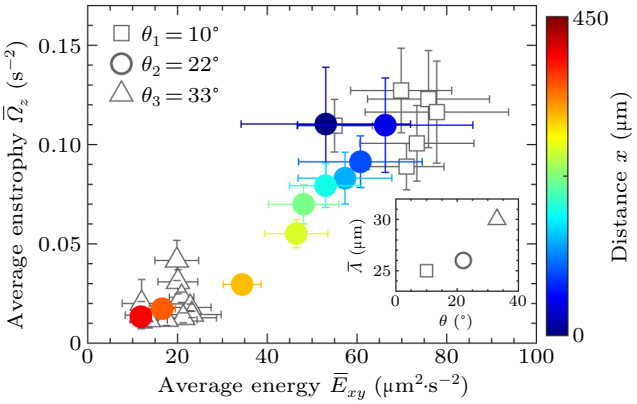


Fig. 5. Relation between spatiotemporal averaged enstrophy $\overline{\Omega}_z$ and kinetic energy $\overline{E}_{xy}$. The typical vortex size, Λ, proportional to $\overline{E}_{xy}/\overline{\Omega}_z$, monotonically depends on the distance. Space averaged $\overline{\Lambda}$ shows monotonic dependence on the contact angle of drops (inset). Error bars indicate standard deviation.

Considering the fact that the confined space at the drop corner can be approximately regarded as a triangle, and the thickness of the liquid film h increases with the distance from the contact line. It has been experimentally confirmed that persistent oxygen-consuming is needed to maintain the mobility

of the bacteria and thus their collective motion.[36,37] It is also quantitatively determined for a accumulation layer of oxygen-rich by combining oxygen diffusion and consumption, chemotaxis, and viscous fluid dynamics.[35] We have measured the active turbulence close to the air–liquid interface. The results show that an outward mean flux towards the contact line, which built a global circulation within this wedge-shape region close to the contact line. We believe that the increasing thickness of liquid film generates a non-uniformity of oxygen distribution, thereby affecting the activity of the bacteria. The dynamical evolution of the oxygen concentration c with the molecular diffusion coefficient of D_c, depends on the bacteria density n, the consumption rate κ of oxygen, and the fluid velocity $\boldsymbol{v}$ as[35]

$$c_t + \boldsymbol{v}\cdot\nabla c = D_c\nabla^2 c - n\kappa f(c). \tag{4}$$

In the present case, the observation is performed minutes after the introduction of the bacterial drop onto the substrate, so that the steady-state is assumed here. We then calculate the thickness h_ℓ of this accumulation layer rich in oxygen by setting Eq. (4) to its steady form and neglecting the inertial effect. With dimensionless function $f(c)\approx 1$ and initial number density n_0 of the bacteria, then $h_\ell = D_n/v_c$,[35] where D_n is the bacterial diffusion constant and v_c is a typical chemotactic velocity. In our case, $D_n = 10^{-5}$ cm^2/s and $v_c = 10$ μm/s. The thickness of accumulation layer of oxygen-rich is then estimated to be $h_\ell \approx 100$ μm. This is in good agreement with the measurement that turbulent kinetic energy decays dramatically at $x\approx 300$ μm with a thickness of ~ 120 μm. Furthermore, by following the similar analysis in Ref. [35], we calculate the spatiotemporal-averaged kinetic energy $\overline{E}_{xy} = \langle(v_x^2+v_y^2)/2\rangle$ and enstrophy $\overline{\Omega}_z = \langle\omega_z^2/2\rangle$, where ω_z is the vorticity in the observation plane. The visual field is divided into equal parts along the radial direction starting from the contact line to the center of the drop. We find that both $\overline{\Omega}_z$ and $\overline{E}_{xy}$ decrease with the growing distance away from the contact line. As shown in Fig. 5, the declining trend observed in the solid circles with gradient color can be attributed to the diminishing activity caused by oxygen depletion, specifically for the case of $\theta = 22°$. Besides, most of the data points are scatteringly gathered in low and high $\overline{\Omega}_z$, $\overline{E}_{xy}$ region in the cases of θ_3 and θ_1 respectively. This collapse of data points is due to the almost constant activity. We then correlate the $\overline{E}_{xy}$ and $\overline{\Omega}_z$ to characterize the length scale by $\Lambda = (\overline{E}_{xy}/\overline{\Omega}_z)^{1/2}$, which is expected to be the same magnitude as the characteristic size of the vortices and is inversely proportional to the slope between $\overline{\Omega}_z$ and $\overline{E}_{xy}$. Additionally, an intriguing observation is that the average ratio of $\overline{\Omega}_z$ to $\overline{E}_{xy}$ demonstrates a consistent inclination towards higher values as the drop contact angle increases. This trend is clearly depicted in the inset of Fig. 5 and is in good agreement with the calculated correlation length. It implies that the balance between $\overline{E}_{xy}$ and $\overline{\Omega}_z$ is controlled by varying the contact angles of the bacterial drops.

2.2. Local anisotropic and global isotropic

In the inertia turbulence, it is realistic anisotropic at the typical scale of the system since the energy is injected from the boundary. While well developed flow is normally regarded as isotropic which is also the essential basis of most statistical theories.[38–40] However, most theoretical and numerical studies for living turbulence also keep this isotropic hypothesis down to the unit-scale regime.[9] It has been shown that a long-wavelength hydrodynamic instability drives the transition to form active turbulence.[41–43] In living turbulence, however, the isotropy or anisotropy is of great interest for evidence. Hence, the local anisotropy of living turbulence in our system is characterized at each node in the viscous field, through the time-averaged product of turbulent velocities $\overline{v_x'\cdot v_y'}$. The red and blue spots in the map shown in Fig. 6(a), represent locally anisotropic with nonzero velocity products and ellipse-like asymmetry with opposite signs in the insets. Although it is locally anisotropic in the living turbulence system, the injected energy can be gathered to form collective motion at a much larger scale due to bacterial interactions. We thus

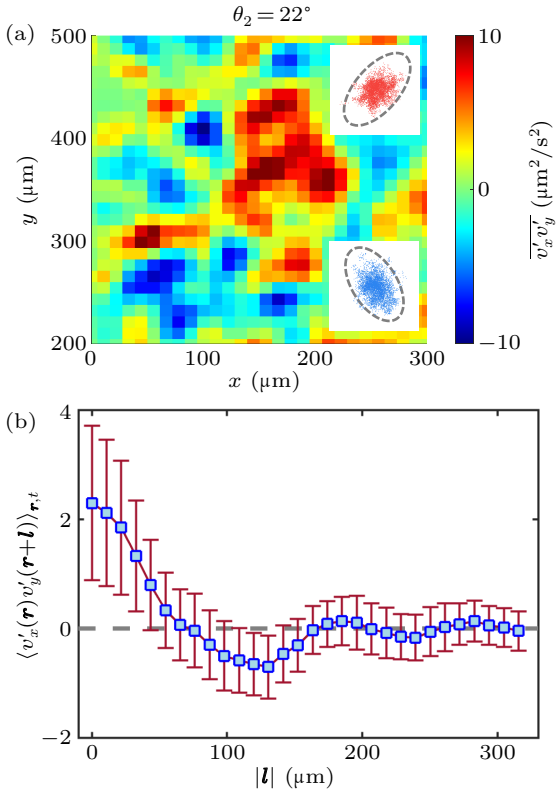


Fig. 6. Local anisotropy at the small scale while isotropy at the global scale. (a) Product distribution of turbulent velocity components. Results are derived from the average of 5000 frames. Red and blue spots indicate anisotropy, whereas green spots show isotropy. Insets (i) and (ii) display the distribution of turbulent velocity components with locally anisotropic features. (b) Turbulent velocity distribution of the whole view and $\overline{v_x'v_y'}\approx 0$ suggests a global isotropy.

analyze the spatiotemporal average of the correlation function of turbulent velocities in given distances. After considering and going through every velocity point in spatial and averaging on 500 frames (time of 10 s), a dependence that changes as the distance $|\boldsymbol{l}|$ increases has been presented in Fig. 6(b). We find that the correlation function is non zero at short distances showing anisotropic properties and declines to a plateau around zero near 70 μm which is in the order of typical size of collective motion. The analysis above reveals that the living turbulence is locally anisotropic due to energy generation at the unit scale and global isotropic at a much larger scale.

2.3. Energy spectrum and scaling

The structure of the swirling flow generated by the bacterial collective motion can be characterized by the velocity correlation functions which are calculated and plotted in Fig. 7. The characteristic size and persistence time of the vortices are calculated to be ~ 50 μm and ~ 2 s as the order of magnitude, respectively. Turbulence exhibits a remarkable dynamical complexity characterized by vortices of varying sizes and random velocity fluctuations. Beneath the chaotic-like velocity field, a universal law called Kolmogorov $-5/3$ scaling has been found to govern the energy cascade in inertial turbulence.

Here, for the 2D living turbulence, the energy spectrum $E(k)$ can be calculated by

$$E(k) = \frac{k}{2\pi} \int \langle \boldsymbol{v}(\boldsymbol{r},t) \cdot \boldsymbol{v}(\boldsymbol{r}+\boldsymbol{R},t) \rangle_{\boldsymbol{r},t,\psi} \, \exp(-\mathrm{i}k|\boldsymbol{R}|) \mathrm{d}|\boldsymbol{R}|, \tag{5}$$

where $\boldsymbol{R}$ represents the position vector between two considered points and k is the scalar wavenumber with a value of k_l defined by the size of a single bacteria. $\langle\cdot\rangle_{\boldsymbol{r},t,\psi}$ represents the average on the spatiotemporal domain and over the unit circle in wavenumber, respectively. Since the energy is injected in an anisotropic way from individual units, we thus check the one-dimensional spectrum from the velocity components v_x' and v_y', as explained in detail in the method section. We find that the 2D energy spectra of the turbulences can be roughly used for simplification as the overall energy spectra of the non-uniform living turbulence. The $k/k_\mathrm{l} \sim 1$ donates the typical length scale of the unit for the energy injection, which is transferred into large vortices with the size of ~ 50 μm (Fig. 7) at a peak in the energy spectrum in Fig. 8. In this region of large wavenumber, the averaged scaling varies from $-1/5$ to -1, depending on the geometric confinement of the systems. It seems that injected energy can be transferred with different efficiency into the vortices with the characteristic length $\lambda_\mathrm{r} \sim 50$ μm due to collective motion, therefore showing herein different decaying slopes in the energy spectra. The sharper decrease (i.e., k^{-1}) in strong confinement (i.e., $\theta = 10°$) shows higher efficiency due to stronger bacterial alignment to form collective motion,

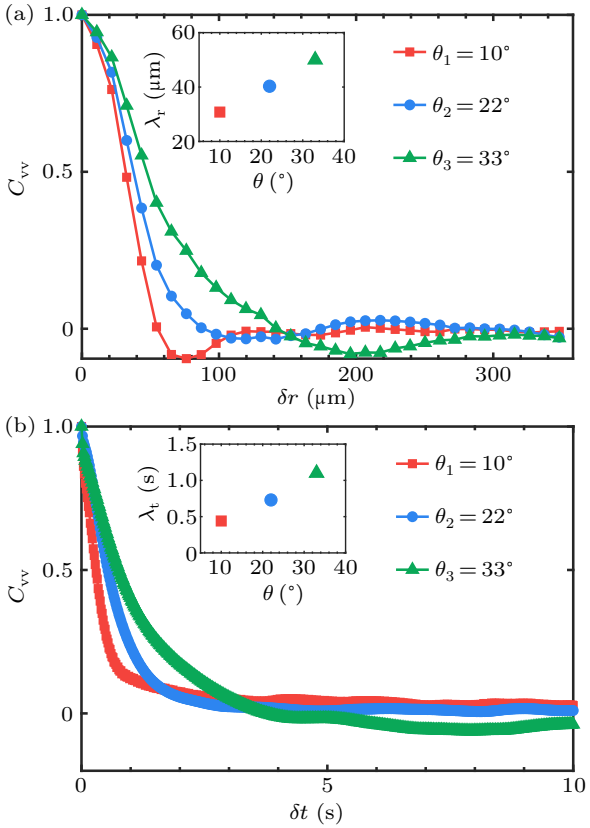


Fig. 7. Correlation length and time of velocity field. (a) Velocity correlation as a function of distance in the focal plane (x–y plane). The correlations for the three cases within drops with different contact angles are calculated based on the extracted velocity field by PIV analysis. Colored lines correspond to the three cases of drop contact angle θ. Shift to a larger correlation length is realized by increasing the contact angle (inset). (b) Time correlations for the three cases show the memory time about 1 s of the order of magnitude. The calculations for spatial and temporal correlations are conducted based on the velocity field measured at the drop regions close to the contact line. Correlation length λ_r and time λ_t are obtained by exponential fitting from $\mathrm{e}^{-\delta r/\lambda_\mathrm{r}}$ and $\mathrm{e}^{-\delta t/\lambda_\mathrm{t}}$. Insets display the dependence of correlation length λ_r and time λ_t on contact angle.

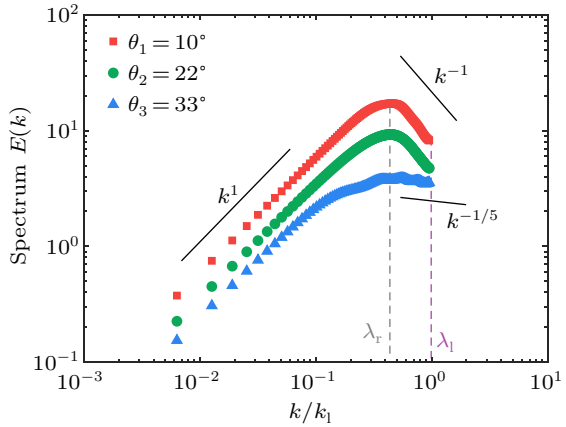


Fig. 8. Energy spectrum analysis in living turbulence. Energy spectra $E(k)$ are plotted for three confinements $\theta_1 = 10°$, $\theta_2 = 22°$ and $\theta_3 = 33°$, where $k_\mathrm{l} = 2\pi/4$ μm^{-1} is the wavenumber for the size of single bacteria. The λ_r indicates the typical vortex size of living turbulence, and λ_l is the typical size of bacteria and corresponds to the scale at which the energy is injected.

than that in loose confinement (i.e., $\theta = 33°$). A robust scaling of k^1 at the small wavenumber is found to be independent of detailed geometric confinement, which is consistent with

result in Ref. [24]. Note that the upper limit of the wavenumber is determined by the typical size of the individual bacteria (λ_l), which is not sufficiently smaller than the characteristic coherent length (λ_r) of the collective motion. Thus, as shown in Fig. 8, calculating the energy scaling in the large range of wavenumber can not be across orders of magnitude.

3. Conclusion

We construct spatial confinements featuring varying thickness gradients by manipulating the contact angle of sessile drops containing dense bacterial suspension. The diffusion-limited layer of oxygen from the air–liquid interface to the bottom of the drop creates a non-uniform oxygen concentration. The approximate cut-off distance of 100 μm is estimated along the height direction, causing the heterogeneous distribution of bacterial activity along the radial direction of drop. The velocity fluctuation shows a large value close to the contact line where the oxygen is rich, while decays inward to the drop center where oxygen supply is significantly reduced due to the diffusion-limited regime across the thick liquid layer. Therefore non-uniform living turbulence is produced. Interestingly, energy is injected in a locally anisotropic way at the unit scale, but generates the isotropic feature at a much larger scale with energy spreading. The heterogeneous turbulence here is governed by the bacterial activity, thereby regulating a global flux of mean kinetic energy. This flux exhibits a linear dependence on the gradient of turbulent energy, analogous to the diffusion law. The bacterial activity can be controlled by the wedge-shaped geometry at the corner of a sessile drop. This natural non-uniform thickness of the liquid layer can tune the balance between $\overline{E}_{xy}$ and $\overline{\Omega}_z$ with a monotonic dependence by varying the contact angles of the bacterial drops. And the finding suggests a potential strategy for controlling energy transfer through the deliberate design of non-uniform living turbulence. Furthermore, we perform a detailed analysis of the energy spectra, revealing a distinct scaling behavior for large wavenumbers ranging from $k^{-1/5}$ to k^{-1}. This scaling variation clearly demonstrates a pronounced dependence on the geometric confinement presents within the bacteria drops. We also characterize the energy spectra and show that the scaling for large wavenumber varies from $k^{-1/5}$ to k^{-1}, and this scaling behavior indicates a significant correlation with the geometric confinement presents within the bacterial drops.

4. Materials and method

4.1. Bacteria

The wild-type bacillus subtilis (strain 168) was used in all experiments. The bacteria were cultured using a standard protocol. In brief, the bacteria was taken out from a frozen tube stored at −20 °C, and then transferred into the Luria–Bertani broth (LB) medium in a plastic tube for overnight growth at 30 °C. Thereafter, a controlled volume of this bacterial suspension was picked and introduced to the new LB medium with a volume of 20 mL in a normal centrifugation tube, in order to keep the final optical density OD ≈ 0.05 measured under the optical wavelength of 600 nm. Then the tube with the mixture of bacteria and medium was kept on a shaker at 30 °C with a shaking speed of 200 rpm for about 6 h. All the culture medium here of LB was made before the experiment from the components of tryptone 1.0%(w/v), yeast extract 0.5%(w/v), and NaCl 1.0%(w/v). The bacterial growth was stopped at the mid of the exponential phase. Then they were harvested and concentrated by centrifugation with the acceleration of 1500 g for 5 mins. After centrifugation, the clear upper supernatant was removed, and then the bacterial pellet was re-suspended into the motility buffer (MB). The MB medium was prepared with 0.01 M potassium phosphate, 0.067 M NaCl, and 10 M EDTA, and was adjusted to pH = 7.0. The suspension was then washed twice by MB and diluted to the expected volume fraction ϕ (here $\sim 7\%$, only accounting for volume occupation by the bacterial head body). The bacteria body length and radius were measured as ≈ 4.0 μm and ≈ 0.5 μm, respectively. Note that the volume fraction of bacteria was roughly calibrated as $\phi = 0.001$ corresponding to the bacterial number density of $n_0 = 8 \times 10^8$ cells/mL or $\mathrm{OD}_{600} = 1.0$.

4.2. Experimental setup

We deposited 5 μL bacteria suspension onto a microscope quartz coverslip by a needle with inner diameter of 0.11 mm, to form a sessile drop. The coverslip and bacterial drop were together enclosed in an acrylic chamber loaded on the stage of the microscopy with saturated humidity and at room temperature ($\sim$ 25 °C) to avoid the influence of evaporation as well as external disturbance. Images were recorded 3 min later than transfer process, in order that a steady state was sufficiently developed within the bacterial drop. An inverted microscope (Nikon Ti2-E, Japan) equipped with high speed camera (Hamamatsu, ORCA-Flash4.0 V3) was used for imaging in the bright-field mode. Two objective lens 20× (NA = 0.45) and 60× (NA = 1.2) were used to obtain the view-filed with size about 696 μm × 695 μm (0.34 μm/pixel) and 225 μm × 225 μm, respectively. The frame rate was fixed to be 50 fps with resolution of 2048 pixels × 2044 pixels. All snapshots and video stacks were focused on the bottom of the coverslip, which was defined as x–y plane in our coordinate system. No evaporation flow was observed in our experiments. The observation window was located in the region near the contact line of the bacterial drop.

4.3. Image processing and data analysis

The continuous image sequences taken by bright-field microscopy, stored the signal intensity of the whole field, which reflected the movement of the coarse-grained flow generated by dense swimming bacteria. The imaging here was difficult for particle-resolved tracking but favored the measurement of the velocity field. This velocity field could be obtained by the analysis routines of PIVlabs in MATLAB based on the raw videos. The key parameters, window size and step size, were set as 128 pixels and 32 pixels respectively for all of our PIV processes. Then, the optimal interrogation window size was calibrated as 43.52 μm by 43.52 μm, for each pair of neighboring frames. Other parameters were set to be default values. The minimum lattice spacing of the velocity field was 10.88 μm. The velocity field in Fig. 1 shows the velocity vectors at each lattice. To verify the accuracy of PIV measurements, we also carried out particle tracking velocimetry (PTV) by adding passive colloidal tracers (1 micrometer of diameter, red fluorescence-labeled, Fluoro–Max, thermo scientific) in bacterial suspensions. The radial velocity distribution $\overline{v}_x$ shows similar results by using both PIV and PTV (Fig. 9), displaying a maximum velocity band located around $x = 300$ μm.

In the quasi-two-dimensional cases or the 2D projection of flows on the observation plane, the turbulence kinetic energy (TKE) is defined as $\overline{E}_{\rm t}(\boldsymbol{r}) = \frac{1}{2}(\overline{v}_x'^2(\boldsymbol{r}) + \overline{v}_y'^2(\boldsymbol{r}))$. With the PIV results, the turbulent velocity components are calculated by the difference between the instantaneous and the average velocity, i.e., $v_x' = v_x - \overline{v}_x$; $v_y' = v_y - \overline{v}_y$. Meanwhile, mean kinetic energy (MKE) is written as $\overline{E}_{\rm m}(\boldsymbol{r}) = \frac{1}{2}(\overline{v}_x^2(\boldsymbol{r}) + \overline{v}_y^2(\boldsymbol{r}))$.

Spatial and time correlation lengths quantify the spatial and temporal velocity correlations, respectively. $C_{\rm vv}(\boldsymbol{\delta r}) = \langle \boldsymbol{v}(\boldsymbol{r}) \cdot \boldsymbol{v}(\boldsymbol{r}+\boldsymbol{\delta r})/\boldsymbol{v}^2(\boldsymbol{r})\rangle_{\boldsymbol{r}}$ is used to calculate the spatial correlation function of velocity, and similarly $C_{\rm vv}(\delta t) = \langle \boldsymbol{v}(t) \cdot \boldsymbol{v}(t+\delta t)/\boldsymbol{v}^2(t)\rangle_t$ for the temporal correlation function. The results of the spatiotemporal correlation of living turbulence under three confinements are shown in Fig. 7.

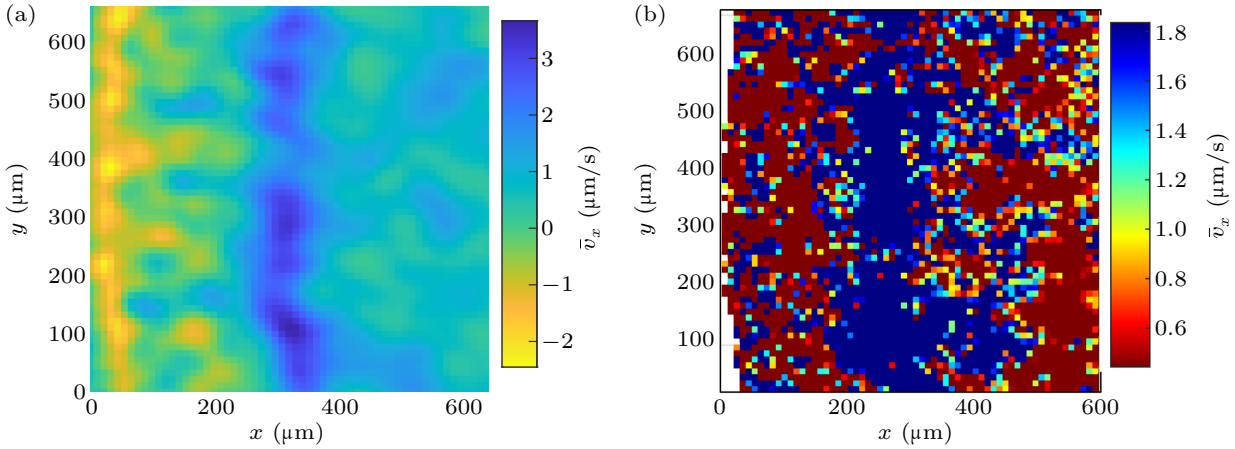


Fig. 9. Consistence of PIV and PTV results on velocity measurements. Panel (a) shows the calculated velocity $\overline{v}_x$ in the radial direction for the bacterial drop at a contact angle of $\theta = 22°$, based on the PIV analysis. Panel (b) shows a very similar result but based on the PTV measurements.

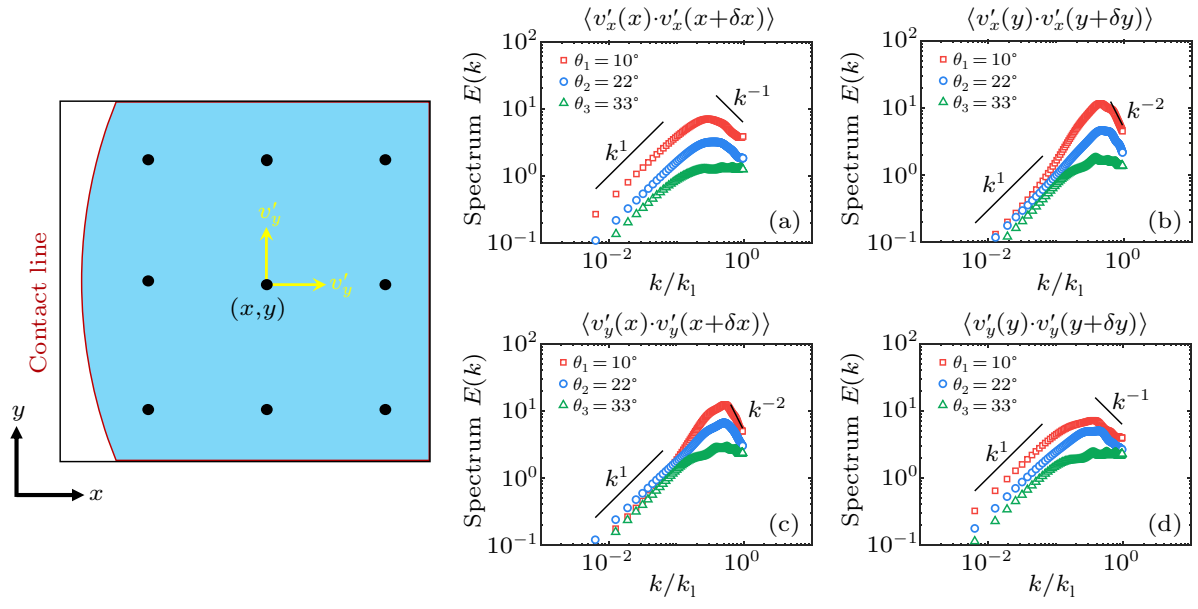


Fig. 10. One-dimensional energy spectra of the turbulent velocity components.

The energy spectra $E(k)$ quantify the energy distribution over different length scales $\lambda = 2\pi/k$, where k is the wave number. Here, the energy spectrum is obtained by calculating the Fourier transform of the two-point velocity correlation function $\langle \boldsymbol{v}(\boldsymbol{r}_0)\cdot\boldsymbol{v}(\boldsymbol{r}_0+\delta\boldsymbol{r})\rangle$, averaging over the spatiotemporal domain and the unit circle in wavenumber space. Here, we check the one-dimensional energy spectra in separate directions except for energy distribution with respect to the scalar wavenumber by averaging around the unit circle. We calculate the turbulent velocity components v'_x and v'_y along x and y axes as $\langle v'_x(x)\cdot v'_x(x+\delta x)\rangle$, $\langle v'_x(y)\cdot v'_x(y+\delta y)\rangle$, $\langle v'_y(x)\cdot v'_y(x+\delta x)\rangle$ and $\langle v'_y(y)\cdot v'_y(y+\delta y)\rangle$, as shown in Fig. 10. We can see that scaling of radial velocity along the radial direction, has the same scaling as that of the total spectrum with scalar wavenumber calculated from 2D velocity. Therefore, the 2D energy spectra of the turbulences can be roughly used for simplification as the overall energy spectra of the non-uniform living turbulence.

Acknowledgments

Project supported by the National Natural Science Foundation of China (Grant Nos. 12174306 and 12004308) and the Natural Science Basic Research Program of Shaanxi (Grant No. 2023-JC-JQ-02). The authors also thank D. Saintillan, A. Lindner, and X. Shi for useful discussions and contributive suggestions.

References

[1] Alert R, Casademunt J and Joanny J F 2021 *Annu. Rev. Condens. Matter Phys.* **13** 1
[2] Ishikawa T, Yoshida N, Ueno H, Wiedeman M, Imai Y and Yamaguchi T 2011 *Phys. Rev. Lett.* **107** 028102
[3] Wensink H H, Dunkel J, Heidenreich S, Drescher K, Goldstein R E, Löwen H and Yeomans J M 2012 *Proc. Natl. Acad. Sci. USA* **109** 14308
[4] Bratanov V, Jenko F and Frey E 2015 *Proc. Natl. Acad. Sci. USA* **112** 15048
[5] Alert R, Joanny J F and Casademunt J 2020 *Nat. Phys.* **16** 682
[6] Dombrowski C, Cisneros L, Chatkaew S, Goldstein R E and Kessler J O 2004 *Phys. Rev. Lett.* **93** 098103
[7] Sokolov A, Aranson I S, Kessler J O and Goldstein R E 2007 *Phys. Rev. Lett.* **98** 158102
[8] Wolgemuth C W 2008 *Biophys. J.* **95** 1564
[9] Dunkel J, Heidenreich S, Drescher K, Wensink H H, Bär M and Goldstein R E 2013 *Phys. Rev. Lett.* **110** 228102
[10] Wu X L and Libchaber A 2000 *Phys. Rev. Lett.* **84** 3017
[11] Kunze E, Dower J, Dewey R and D'asaro E 2007 *Science* **318** 1239
[12] Kurtuldu H, Guasto J S, Johnson K A and Gollub J P 2011 *Proc. Natl. Acad. Sci. USA* **108** 10391
[13] Zaid I M, Dunkel J and Yeomans J M 2011 *J. Royal Soc. Interface* **8** 1314
[14] Taylor J R and Stocker R 2012 *Science* **338** 675
[15] Houghton I A, Koseff J R, Monismith S G and Dabiri J O 2018 *Nature* **556** 497
[16] Mukherjee S, Singh R K, James M and Ray S S 2021 *Phys. Rev. Lett.* **127** 118001
[17] Linkmann M, Boffetta G, Marchetti M C and Eckhardt B 2019 *Phys. Rev. Lett.* **122** 214503
[18] Martínez-Prat B, Ignés-Mullol J, Casademunt J and Sagués F 2019 *Nat. Phys.* **15** 362
[19] Li H, Shi X Q, Huang M, Chen X, Xiao M, Liu C, Chaté H and Zhang H 2019 *Proc. Natl. Acad. Sci. USA* **116** 777
[20] Liu Z, Zeng W, Ma X and Cheng X 2021 *Soft Matter*
[21] Vicsek T and Zafeiris A 2012 *Phys. Rep.* **517** 71
[22] Vicsek T, Czirók A, Ben-Jacob E, Cohen I and Shochet O 1995 *Phys. Rev. Lett.* **75** 1226
[23] Chaté H, Ginelli F, Grégoire G, Peruani F and Raynaud F 2008 *Eur. Phys. J. B* **64** 451
[24] Martínez-Prat B, Alert R, Meng F, Ignés-Mullol J, Joanny J F, Casademunt J, Golestanian R and Sagués F 2021 *Phys. Rev. X* **11** 031065
[25] Mukherjee S, Singh R K, James M and Ray S S 2021 *Phys. Rev. Lett.* **127** 118001
[26] Bárdfalvy D, Nordanger H, Nardini C, Morozov A and Stenhammar J 2019 *Soft Matter* **15** 7747
[27] Čopar S, Aplinc J, Kos Ž, Žumer S and Ravnik M 2019 *Phys. Rev. X* **9** 031051
[28] Krajnik Ž, Kos Ž and Ravnik M 2020 *Soft Matter* **16** 9059
[29] Shendruk T N, Thijssen K, Yeomans J M and Doostmohammadi A 2018 *Phys. Rev. E* **98** 010601
[30] Varghese M, Baskaran A, Hagan M F and Baskaran A 2020 *Phys. Rev. Lett.* **125** 268003
[31] Guillamat P, Ignés-Mullol J and Sagués F 2017 *Nat. Commun.* **8** 564
[32] Lin S Z, Zhang W Y, Bi D, Li B and Feng X Q 2021 *Commun. Phys.* **4** 21
[33] Gagnon D A, Ran R and Arratia P E 2021 arXiv: 2111.00068
[34] Thielicke W and Stamhuis E 2014 *J. Open Res. Softw.* **2** e30
[35] Tuval I, Cisneros L, Dombrowski C, Wolgemuth C W, Kessler J O and Goldstein R E 2005 *Proc. Natl. Acad. Sci. USA* **102** 2277
[36] Douarche C, Buguin A, Salman H and Libchaber A 2009 *Phys. Rev. Lett.* **102** 198101
[37] Tejera F, Libchaber A and Petroff A P 2018 *Phys. Rev. E* **98** 042409
[38] Kolmogorov A N 1941 *Cr. Acad. Sci. URSS* **30** 301
[39] Van Atta C 1991 *Proc. Math. Phys. Eng. Sci.* **434** 139
[40] Pope S B 2000 *Turbulent Flows* (Cambridge: Cambridge University Press)
[41] Saintillan D and Shelley M J 2008 *Phys. Rev. Lett.* **100** 178103
[42] Saintillan D and Shelley M J 2015 *Complex Fluids in Biological Systems* (Berlin: Springer) pp. 319–355
[43] Hohenegger C and Shelley M J 2010 *Phys. Rev. E* **81** 046311